Computers & Fluids 82 (2013) 1–13

Contents lists available at SciVerse ScienceDirect

Computers & Fluids

journal homepage: www.elsevier.com/locate/compfluid

CFD simulations of turbulent buoyant atmospheric flows over complex geometry: Solver development in OpenFOAM

Federico Flores *, René Garreaud, Ricardo C. Muñoz

Departamento de Geofísica, Universidad de Chile, Santiago, Chile

ARTICLE INFO

Article history:
Received 3 July 2012
Received in revised form 11 April 2013
Accepted 28 April 2013
Available online 15 May 2013

Keywords:
CFD
OpenFOAM
LES
Wind engineering

ABSTRACT

This paper, first of a two-part work, presents an overview of the development of a computational fluid dynamics (CFD) solver in OpenFOAM platform to simulate the internal ventilation regime within an open pit including the effects of developed turbulence, buoyancy and stratification. To incorporate the effect of stratification in the simulations we have chosen a formulation that includes density as a variable in the system of equations, thus facilitating further study of buoyant flows. Given the importance of turbulence in this type of large-scale flows we have used Large Eddy Simulation (LES) to incorporate it in the calculation, using a Detached Eddy Simulation (DES) approach to solve the flow near walls. Specific initial and boundary conditions were defined.

The results presented in this paper, including several tests of the solver where we compared our results with experimental or numerical data, have demonstrated the validity of using OpenFOAM to study this type of complex multiphysics problems. Especially advantageous in this regard are the flexibility provided by the modular structure of the code, the possibility of defining specific boundary and initial conditions for each case, and the ability of generating detailed meshes of complex geometries. Also we probed the benefits of using a DES approach, allowing us to solve developed turbulence and the interaction of the flow with detailed geometry. A second paper associated to this work will expose the application of the solver to large open pit mines, simulating the particular case of Chuquicamata, one of the largest open pit mines in the world, located in northern Chile.

1. Introduction

In recent years, a growing interest has been seen in applying Computational Fluid Dynamics (CFD, for acronyms see Appendix A) to simulate complex micrometeorological processes, like air flow in urban areas, over complex topography, or that controlled by thermal gradients [1–4]. Among several factors that have contributed to this interest is the application of CFD to new fields, such as renewable energies, the dispersion of contaminants or the study of natural ventilation systems. In general, the problem can be described in terms of the interaction, within the atmospheric boundary layer, between the airflow and the objects that define the complex surface geometry.

A main challenge of the numerical simulation of atmospheric flows arises from the different spatial scales involved, ranging from the small scale typically used in engineering to the large scale used in meteorology. The DNS technique, in which the Navier–Stokes equations are numerically solved without any turbulence model, allows to study the turbulence in detail [5], but its computational requirements restrict it to small domains with reduced geometrical complexity. This makes it incompatible with the study of wind around complex geometries, in which case less expensive techniques using time averaged equations (RANS) are preferred [2] and specialized in the treatment of walls [6]. To simulate the circulation in valleys or to study the turbulence within the convective boundary layer, it is preferable to opt for LES techniques [7–9], that can resolve large scale vortices more accurately than RANS, although they are difficult to apply to complex geometries [10]. In general, the techniques used in meteorological large scale problems [11,12] employ numerical methods that make difficult for these models to resolve the interaction of the flow with small scale obstacles, in spite of using refined meshes [13]. They typically use standard finite-difference methods, which lack the geometric flexibility offered by finite volume methods used in CFD. These methods employ relatively low-order numerical approximations. This, for example, explains the problems when using WRF (Weather Research and Forecasting) in urban areas and the need of coupling it with CFD models that are capable of resolving urban-scale flows [14].

There is a consensus in the need that both approaches explained above (importance of walls and developed turbulence) converge to achieve more realistic simulations of the flows that characterize the Atmospheric Boundary Layer (ABL), in particular close to the

* Corresponding author. Tel.: +56 2 29784562.
E-mail address: federico@dgf.uchile.cl (F. Flores).

0045-7930/$ - see front matter © 2013 Elsevier Ltd. All rights reserved.
http://dx.doi.org/10.1016/j.compfluid.2013.04.029

ground, where most human activities take place. It is necessary to consider that close to the surface the energy-containing turbulence scale may be close to the scale of the spatial filter used in the LES equations, which could lead the simulation to operate in a range that moves away from the optimum for which LES was designed (“Terra Incognita” [13]). To solve this problem new subgrid models have been developed for LES, as well as hybrid techniques that are capable of adapting to different scales, combining RANS with LES models. *Detached Eddy Simulation* (DES) techniques solve near-wall regions in a RANS-like manner, and the rest of the flow in a LES-like manner [10,15].

To simulate the air circulation of interest to us, which involves several physical processes interacting between each other and with a complex geometry, it is necessary to use computational tools that are capable of incorporating these processes and complex meshes. In our case, given the great versatility that it provides, we selected the CFD tool *OpenFOAM* (Open Field Operation and Manipulation [16]) as development platform, focusing the problem from a multi-physical perspective, incorporating the effects of buoyancy and turbulence. It is within the efforts described in the previous paragraph where we can place this research, focusing on using *OpenFOAM* as a development platform for DES type models that incorporate buoyancy and stratification in the study of atmospheric flows, but resolving the flow around complex geometries.

We aim our application towards the modelling of atmospheric circulation within open pit mines, with the objective of applying it to study the complex circulation and dispersion of contaminants that originates within Chuquicamata, one of the largest open pit mines in the world, whose ventilation seems to be dominated by convective effects [17]. The pit, located in northern Chile (22°17′20″S 68°54′W, about 3000 m ASL), measures 4 km long, 3 km wide and 1 km deep, and has a complex topography. Particulate matter is almost always present, as well as air currents produced by natural convection, leading to a strong contamination inside and outside the pit.

The structure of this first part of the work, that describes the development of the solver, consists of a first section where we briefly describe the numerical treatment used to deal with the physical problem, describing the governing equations and the initial and boundary conditions considered. After that we present several cases in which we applied the solver and compared its results with values measured or documented in other works. This stage follows a logical progression, from relatively simple problems up to more complex ones that incorporate multiphysics simulation. Upon finishing we include a review of the main conclusions of the work, discussing the strengths and weaknesses of the solver, its possible applications and improvements that could be incorporated to it in the future. We leave for a second paper the application of the solver to open pit mines, including the particular case of Chuquicamata.

2. Physical problem and model description

2.1. Physical problem

In general the type of atmospheric circulation that we study comprises two main processes that dominate its evolution:

- Mechanical effects caused by the topographic or structural obstacles with which the flow interacts, leading to acceleration or recirculation zones.
- Buoyancy effects caused by the heat flux from or towards the surface, which can generate important vertical air flow accelerations. These convective effects depend on the stability of the atmosphere, so that stratification must be taken into account.

Both processes interact with each other, and are directly influenced by the intense turbulence that characterizes many environmental flows. As we saw, this obligates us to widen the range of scales considered from those used in the study of urban wind to those used in the analysis of atmospheric turbulence, making it necessary to use techniques that are able to work on this range of scales.

2.2. Solver

As already mentioned, to address the problem we have selected the CFD toolbox *OpenFOAM*. Although we used as a base the solver *buoyantPimpleFoam* available in the 1.7.1 version of *OpenFOAM*, we modified it to better adapt to our problem. Furthermore, we included specific boundary and initial conditions necessary to deal with the problem in question. We will detail the development of our solver in next sections.

2.2.1. The OpenFOAM framework

OpenFOAM is a collection of C++ libraries designed to solve complex problems in fluid mechanics. Developed with the desire of obtaining a more effective numerical platform than Fortran, it has benefitted from the new C++ object-oriented programming functionality. Its completely free distribution and the flexibility it offers allow the development of specific solvers by the user, which can be integrated with already existing tools. As most of the CFD codes currently used in engineering, it uses a finite volume formulation. Within its libraries, *OpenFOAM* integrates turbulence models (RANS and LES), thermophysical models, radiation models and wall functions, which can be accessed when developing a solver. Furthermore, the code offers the functions of integrating complex geometries in the calculation, through the use of the *snappyHexMesh* tool. For an extensive review of the numerical methods used by the code, as well as of the available tools, we refer to the available documentation [18].

There are several examples of the application of *OpenFOAM* to the study of atmospheric flows. García and Boulanger [19] simulated the wind flow over Mount Saint Helens in the United States employing *OpenFOAM* with a standard k–ε RANS turbulence model. A similar work was done by Hussein and El-Shishiny [20] studying the wind flow over the Giza Plateau in Egypt. García et al. [21] simulated the convective winds generated in the Aburra open valley, near Medellín, Colombia, using standard k–ε RANS turbulence. Pedruelo [22] used *OpenFOAM* to model the non-buoyant wind flow over complex terrain using RANS turbulence models with wall functions, to make accurate predictions of wind power production. Churchfield et al. [23] developed an *OpenFOAM* solver using LES to simulate buoyant flows under the Boussinesq approximation, focusing on the flow interaction with wind turbines. There is apparently no record that *OpenFOAM* has been used to study the circulation caused by buoyant flows within closed valleys with complex topography or obstacles, as open pit mines. In particular, there is no evidence that the new compressible solvers that consider density as a variable of calculation (instead of using the Boussinesq approximation), using a DES approach, have been used for these applications. Our interest lies in studying the problem using this new approach, that allows integrating buoyancy, stratification, turbulence and complex geometry in one single model, with the aim of applying it to the particular case of ventilation within large open pit mines. The DES approach allows us to include complex topography in the analysis, while the explicit inclusion of density variations improves the treatment of stratification and buoyancy effects.

2.2.2. Governing equations and implementation in OpenFOAM

Given the need to incorporate stratification into the model, we use a quasi-compressible approximation, including density as an explicit variable in the calculation. A detailed view of the algorithms used in *OpenFOAM* to couple pressure and velocity in

the compressible case (PISO type algorithms, *Pressure-Implicit with Splitting of Operators*), can be found in [24–27].

When we apply LES, we assume that any variable (f) is decomposed into two components, one large-scale ($\bar{f}$) and the other small-scale (f'), i.e.:

$$f = \bar{f} + f' \tag{1}$$

A filtering operation is used to extract the large-scale components, consisting of a convolution with a previously defined function:

$$\bar{f} = \oint G(x, x'; \Delta) f(x') dx' \tag{2}$$

where Δ, the filter width, generally depends on the mesh. There are different alternatives for the function G, depending on the numerical discretization to be used. The approach employed by LES is to directly solve the large scale flow while modelling the effect of the small scales, which will be in general subgrid. There are different SGS (subgrid scale) models to do this. For a description of the manner in which LES is applied in *OpenFOAM* and in the SGS models available, see for example [28].

In our case, considering compressibility effects, we must use a filtered version of the general continuity equation (for simplicity we will not include bars above large-scale variables):

$$\frac{\partial \rho}{\partial t} + \nabla \cdot (\rho \vec{U}) = 0 \tag{3}$$

The momentum equation corresponds to the filtered Navier–Stokes equation:

$$\frac{\partial}{\partial t}(\rho u_i) + \frac{\partial}{\partial x_j}(\rho u_i u_j) - \nabla \cdot (\mathbf{T} + \mathbf{T}_{sgs}) = -\nabla p + \rho \vec{g} - \nabla p^* + \vec{f}_c \tag{4}$$

where $\mathbf{T}$ represents the stress tensor associated with molecular viscosity, μ:

$$\mathbf{T} = \mu \left[\left(\frac{\partial u_i}{\partial x_j} + \frac{\partial u_j}{\partial x_i} \right) - \frac{2}{3} \left(\frac{\partial u_k}{\partial x_k} \right) \delta_{ij} \right] \tag{5}$$

while $\mathbf{T}_{sgs}$ is the Subgrid-Scale stress (SGS) tensor, which will be calculated using one of the subgrid models. For the latter, *OpenFOAM* offers different alternatives. In general, a model is used to estimate a subgrid turbulent viscosity μ_{sgs}. In this work we used one equation SGS model [29].

The term ∇p^* in (4) corresponds to an external force used to maintain the flow. When using cyclic boundaries this is done, for example, computing ∇p^* such that the mass flow rate is constant. When using periodic boundaries this term is used to include a body force. Although in (4) we include Coriolis ($\vec{f}_c = -2\rho\vec{\Omega} \times \vec{U}$), in many simulations we do not consider it, to focus on the effect of the other physical processes that control the flow and to simplify the simulation configuration. Furthermore, the Coriolis effect would be very weak in the majority of the cases that we are interested in analyzing. The great advantage of *OpenFOAM* is that each one of the above terms can easily be incorporated or eliminated from the solver that is used for each simulation, given that each application can be compiled independently.

The thermal analysis is incorporated through an enthalpy equation [30],

$$\frac{\partial}{\partial t}(\rho h) + \nabla \cdot (\rho \vec{U} h) - \nabla \cdot (\alpha_t \nabla h) - rad = \frac{Dp}{Dt} \tag{6}$$

Among the benefits of using enthalpy ($h = e + pv = f(T,p)$) as a variable is the relative simplicity with which mixtures of variable composition can be incorporated into the model, which is a useful characteristic if in the future we include humidity [31]. In (6), the effective SGS thermal diffusivity, α_t, is equal to the sum of the molecular thermal diffusivity, α, and the subgrid scale turbulent thermal diffusivity, α_{sgs}, i.e.:

$$\alpha_t = \alpha + \alpha_{sgs} \tag{7}$$

The value of α_{sgs} is estimated from the subgrid turbulent viscosity μ_{sgs} (calculated by the SGS model) through the Prandtl turbulent number (Pr_t):

$$\alpha_{sgs} = \frac{\mu_{sgs}}{Pr_t} \tag{8}$$

There is evidence that in the stratified cases the calculation of α_{sgs} should depend on the level of stratification (in general the Prandtl number is modified as a function of the level of stratification [32,33]). However, in this case we have used a fixed value of Pr_t (0.7), trusting that the effect of subgrid turbulence on the calculation is minor. The subject of subgrid turbulent heat transfer is still an area of uncertainty in CFD [34,35].

In the enthalpy Eq. (6) we have included a term associated with radiative transfer (*rad*), which considers the use of the radiation models available in *OpenFOAM* (Finite Volume Discrete Ordinates Model and P1 Method of Spherical Harmonics [36,37]). Divergence of radiation is important in the nighttime close to the ground, favoring rapid cooling [38]. Although we tested this effect when simulating some simple cases, in general we did not activate radiation in the more complex cases, fundamentally due to the high computing cost of incorporating it and because we are mostly interested in daytime conditions.

We used the ideal gas state equation to close the description of the state of the flow:

$$p = \rho R T \tag{9}$$

with R = 287 J/(Kg K). It is interesting to indicate that in *OpenFOAM* this equation is not incorporated in the files that define the model, as the previous equations, but it is defined when the simulation is prepared through the use of the thermophysical libraries provided by the code.

To include passive scalar transport in the model, we use

$$\frac{\partial \rho C}{\partial t} + \nabla \cdot (\rho C \vec{U}) - \nabla \cdot (\alpha_t \nabla C) = f_v \tag{10}$$

where C is the concentration of the scalar and f_v is a source that we wish to include. We use α_t to approximate effective SGS diffusivity, as with the enthalpy equation, since it is usually accepted that this property is part of the flow and applicable to any property that diffuses within it (Schmidt number $\sim$ Prandtl number in gases [39]). Although the molecular diffusivity of the scalar might be very different than that of the enthalpy, the problem is minor because in DES these contributions might be very small.

In summary, the solver includes the following equations: continuity, momentum conservation (Navier–Stokes), enthalpy conservation, ideal gas state and passive scalar transport, using the libraries and tools provided by *OpenFOAM* to solve them (thermophysical, turbulence and finite volume libraries).

2.2.3. Geometry and meshing

Given our interest in working with complex geometries, we used the *snappyHexMesh* tool to solve the problem of mesh generation. *SnappyHexMesh* proved to be very versatile when applied to different domain configurations [40]. In particular, it allows STL files to be used as precursors to mesh generation, making it possible to include complex geometrical forms and even topography in the simulations. In the majority of cases we used the free CAE software *Salome* to generate the necessary STL files. The meshes consisted of hexahedra (hex) and split-hexahedra (split-hex) cells. In cases with complex geometry the mesh was refined near the walls to produce cells with wall normal dimensions between $y_1^+ = 10$ and $y_1^+ = 300$ adjacent to the surface. However, it is impossible to satisfy this criteria everywhere when processes of flow separation and attachment occur.

2.2.4. Initial and boundary conditions

In CFD the initial and boundary conditions used are of fundamental importance, because they directly affect the evolution of the simulation and must necessarily take into account the physical processes that we are modelling. Although *OpenFOAM* offers a wide variety of pre-defined conditions, in the majority of case, it is necessary to create specific conditions for each simulation. Furthermore, there exist important differences whether the simulation considers buoyant effects or not, or whether LES or URANS models are used for turbulence. As we focused on DES buoyant simulations we will describe in detail these conditions, while also presenting non-buoyant URANS and DES conditions as reference:

(a) URANS.

There are different alternatives to define the inlet velocity profile, depending on the information available. If we have experimental data, we can use the expression:

$$U(z) = \frac{U_*}{\kappa} \ln\left(\frac{z-d}{z_o}\right) \tag{11}$$

where U_* (friction velocity), d (displacement height) and z_o (roughness height) are known or can be estimated from data.

If detailed data is not available, we can use a simple power law up to 300 m, such as that suggested in [41], and maintain the velocity fixed at higher altitudes:

$$U(z) = U_s\left(\frac{z}{z_s}\right)^n \tag{12}$$

where U_s is the velocity we want to have at height z_s, and $n \sim 0.25$. In URANS simulations this profile is maintained fixed as a forcing during the entire simulation. We also need to define the turbulence kinetic energy and dissipation rate at the inflow boundary, using expressions like those developed in [42]. The outlet profile of velocity is defined as zero gradient, assuming a fully developed flow. Lateral and top boundaries are defined as stress-free wall: normal component and gradients of tangential components of velocity equal to zero.

(b) Non-buoyant DES.

If we use DES it will be necessary to slightly modify the conditions described above. In particular, the inlet profile of velocity must be perturbed to favor turbulence, for which there are different techniques [43,44]. In *OpenFOAM* it is possible to use the mapping technique to perturb the initial profile, in which a preliminary cyclic computation section coupled into the main calculation is used to give origin to the turbulent perturbation [45]. This was the technique used in this work. Also there exist techniques that numerically generate appropriate turbulent inflows and are relatively easy to implement [44].

(c) Buoyant DES.

In most complex cases, where we incorporate DES as well as buoyancy through changes in density, it is necessary to use cyclic boundary conditions in all the lateral boundaries, in both directions. This is needed to correctly simulate the heat flux from surface, since in the atmosphere it can be assumed that it is released from an infinite surface. To avoid initial compressibility effects, it is also recommended that the simulation be started setting a variable vertical profile of velocity (as described in Eq. (11) or (12)) but mainly uniform throughout the domain (to avoid an inlet flow). Given that when using cyclic boundaries we cannot set the velocity at entrance, it will be necessary to use an external force (as in Eq. (4)) to ensure that the mean velocity aloft is maintained. This force must be incorporated into the code in such a way that it adjusts during the simulation to reduce velocity variations of the mean flow aloft. When defining an initial velocity profile in the entire domain we can favor the development of turbulence close to the ground perturbing the profile there. To do this we introduce periodic perturbations along the x and y-axes through sine and cosine functions [28].

Attention must be paid to configuring the vertical pressure profile in accordance with the potential temperature profile used, to ensure the initial balance of the system. For example, if using an initial potential temperature profile of the following form on a layer of the domain:

$$\theta = \theta_1 + \lambda\,(z - z_1) \tag{13}$$

we use the system of equations:

$$\frac{\partial p}{\partial z} = -\rho g \quad p = \rho R T \quad \theta = T\left(\frac{p_o}{p}\right)^{R/c_p} \tag{14}$$

to obtain:

$$p(z) = \left(p_1^{R/c_p} - \frac{g p_o^{R/c_p}}{\lambda c_p} \ln\left[1 + \frac{\lambda}{\theta_1}(z - z_1)\right]\right)^{c_p/R} \tag{15}$$

which we use to define the pressure profile within the sub-layer in question.

In *OpenFOAM*, when boundary conditions are defined, there are in general two available alternatives: to set the value of the variable in the surface or to set its gradient. Unfortunately, when the heat flux is defined at the walls, neither of the two alternatives is a good choice. The value of the coefficient of effective SGS thermal diffusivity, that controls the subgrid calculations that dominate close to walls, evolves along with the variations in the flow, and therefore we cannot prescribe the heat flux unless we take into account the possible local variations of this coefficient. To avoid this problem we defined specific boundary conditions that use the value of α_t (Eq. (7)) to estimate the temperature gradient necessary to obtain the required heat flux. This temperature gradient is then employed to compute the temperature imposed as boundary condition. Through simple simulations, where we set a surface flux and calculated the total energy transferred to the domain in a determined amount of time, it was possible to clearly verify the proper functioning of this type of boundary condition.

2.2.5. Treatment of walls

OpenFOAM offers a series of specialized libraries to define the boundary conditions on a surface. It has been shown [2,4,6] that in the case of complex configurations that include a set of buildings or obstacles, it is preferable to use a smooth wall condition, given that a rough wall model requires a large grid, which makes it difficult to capture the details of the flow in complex geometries. Because our final motivation was to simulate the flow inside open pits with complex topographies and structures, we focused on using a mesh that includes the topography inside the pit, instead of using surface roughness. Although different works have shown rough walls to be crucial in maintaining the correct ABL profiles along the upwind fetch, in this work any effect of the surface roughness is assumed to be small compared with the effects of the terrain, as suggested in [46].

There are many considerations to take into account when using wall functions in RANS simulations, considering the advantages and limitations of each wall model. For an extensive review, see Blocken et al. [42].

In the case of LES simulations the treatment of the flow close to the walls is especially complex, since, in general, the computational cost of applying this technique in these areas is too high, seriously limiting its application in the case of complex geometries [13,47].

However, the excellent results obtained when LES is applied to areas of flow separation, where most RANS techniques fail, have led in the past few years to the development of a series of hybrid techniques. The DES technique (detached-eddy-simulation), originally proposed by Spalart [15] to deal with highly separated flows such as those existing in the aerospace industry, combines the benefits of LES and RANS, dividing the domain according to different turbulence zones, as shown in Fig. 1. These characteristics make DES especially useful in the case of atmospheric flows around complex geometries, allowing us to benefit from the excellent LES results in zones with highly developed turbulence far from the ground, and from the RANS methods widely used in wind engineering near walls. For a review of the wall functions available in *OpenFOAM*, as well as the DES techniques used in the code, refer to [28]. The results shown in this work correspond to DES simulations using Spalart Allmaras model for the near-wall treatment, although we also experimented with different standard wall functions using URANS simulations to compare results.

2.2.6. Computing support

The development of the model, the configuration of the simulations, and the analysis of the results were done on a personal workstation, running *OpenFOAM* and the *Paraview* viewer. Due to the high computing requirements of the simulations, with domains exceeding 5 million cells, their execution was done in parallel in the Levque cluster of the National Laboratory for High Performance Computing (NLHPC) of the Center for Mathematical Modeling of the University of Chile. The Levque cluster is an IBM iDataplex machine with 536 cores, equipped with Intel Nehalem processors, an Infiniband QDR switch and different development tools [48]. Different *OpenFOAM* scaling tests [49] were carried out in the cluster, one of which is presented in Fig. 2. Since the scaling depends on different factors, such as the complexity of the geometry used in the domain, the type of decomposition used, or the turbulence models selected, the results of Fig. 2 are only referential.

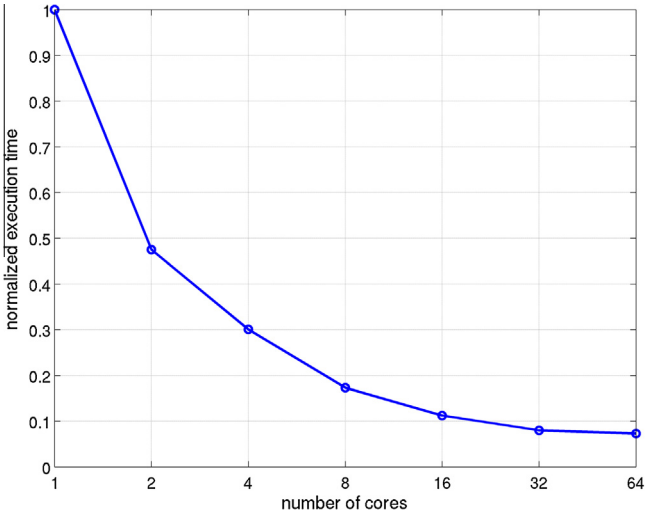

Fig. 2. *OpenFOAM* scalability in cluster Levque, execution time v/s number of cores used.

3. Results and discussion

Considering the complexity of the problem to be addressed, with several physical processes interacting in a complex geometry, at different scales, as we moved forward in our work we chose to perform different levels of validation at each stage of solver development. The logic followed in this process was to gradually incorporate processes to the simulation. We began with a simple case of atmospheric flow around a single obstacle, then we used complex geometries of small and large-scale, and finally we incorporated buoyancy, first with a simple experimental case and then with a well documented atmospheric case. At each stage we compared our results with available data or other simulation efforts. The results shown in each case correspond to DES simulations with OneEquationEddy as the SGS model and Spalart Allmaras wall treatment, although we also performed several URANS simulations with RNG k–ε turbulence model in order to compare the perfomance of both techniques. A fully second-order method in space was used for all simulations. A second order implicit method (backward differentiation) was used for the time integration. We used linear and limited linear differencing schemes for convective terms approximation. Two correctors were set for a PISO loop and 0, 1 or 2 correctors (depending on the complexity of the mesh) for non-orthogonal corrections. Preconditioned (bi-) conjugate gradient method with incomplete-Cholesky preconditioner was used for solving the linear systems with a local accuracy of 10^{-6} for all dependent variables at each time step. In cases with simple geometry we used the mesh generation utility *blockMesh* to create meshes of hexahedral cells in 3-D (*polyMesh* in *OpenFOAM* [18]), changing the grid size by changing the number of cells in each direction. In cases with complex geometry we used the toolbox *snappyHexMesh* to modify a previously defined *blockMesh* mesh (background hex mesh) and adapt it around complex surfaces defined by means of a STL file, creating hexahedra (hex) and split-hexahedra (split-hex) cells. In these cases the grid resolution was adjusted changing the minimum and maximum refinement level in the *refinementSurfaces* dictionary, and modifying the number of patch smoothing iterations before finding correspondence to a surface with the *snapControls* sub-dictionary. In all cases the meshes generated were tested by means of the *checkMesh* utility.

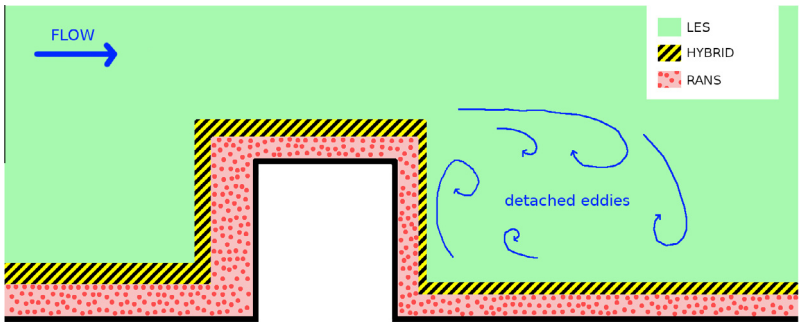

Fig. 1. Typical turbulence zones in a DES simulation, adapted from [28].

3.1. Interaction of the flow with obstacles

In the first stage of model development we were interested in studying the interaction of the flow with complex geometries, so we focused on the use of wall treatment models and the generation of complex meshes. In this early stage we did not consider buoyancy effects, so a simplified version of the solver developed in Section 2.2 was used, which did not include any thermal effect (enthalpy Eq. (6) was not included). In these non-buoyant cases we used initial and boundary conditions as those described in Section 2.2.4 (non-buoyant URANS and DES). As the performance of *OpenFOAM* on non-buoyant turbulent flows around experimental obstacles has been studied in previous works [28,50], we will center our attention on complex large scale geometries and buoyant cases, in order to leave the main text more concise, and we will not include the results of our first experiments using well documented experimental data. Nevertheless, these cases worth a mention due their usefulness as well documented test cases: case 84 from ERCOFTAC library (Turbulent Boundary Layer Flow Over a Cube [51,52]), and the database of the Architectural Institute of Japan AIJ (flow around a rectangular obstacle [53] and a set of 9 obstacles [54,55]). Results from this last case, that allows a good validation of our DES simulations around complex geometries and the use of the *snappyHexMesh* tool to generate fully operational complex meshes, are included in Appendix B.

In order to test the versatility of the *snappyHexMesh* tool in generating complex large-sized meshes, such as those we are interested in working with, and to analize how these meshes interact with the numerical methods available in *OpenFOAM*, we used a complex configuration as study case. This geometry corresponds to a simplified version of the buildings of the School of Physical and Mathematical Sciences of the University of Chile (FCFM), Fig. 3. We used a mesh generated by *snappyHexMesh* and we performed different simulations changing the incident wind direction (southwest, west and northwest wind). The grid exceeded 3 million cells, refined close to the buildings ($\Delta < 1$ m), and was chosen after several mesh tests until obtaining solutions independent of domain size and mesh. The mesh was refined near walls, by the use of *snappyHexMesh* controls, to produce cells with wall normal dimensions between $y_1^+ = 10$ and $y_1^+ = 300$ adjacent to the surface. We simulated 3 h (until reaching a statistically stationary flow) with a time step of 0.05 s, using inlet conditions as those described in the non-buoyant cases of Section 2.2.4. The inlet profile of horizontal velocity was assumed to be distributed as a power law in the vertical direction with the index $P = 0.25$ (Eq. (12)), with a representative velocity of 2 m/s at a reference height of 3 m. The initial inlet boundary for subgrid k is not simple and is unknown. We fixed an inlet value of 0.001 m^2/s^2, trusting that it would be adjusted quickly once the simulation starts. The values of velocity and k were perturbed using the mapping technique described previously and available in *OpenFOAM*.

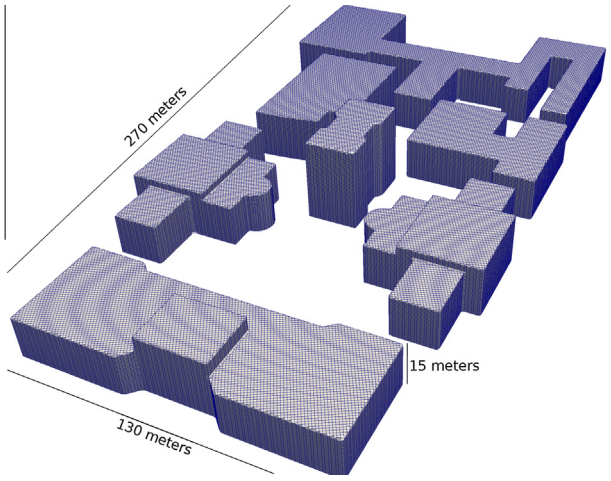

Fig. 3. FCFM building complex generated by using the *snappyHexMesh* tool. Mesh refined close to the buildings.

The last hour average results for a southwest wind, the most common condition in this location, are shown in Fig. 4, which corresponds to a plane 3 m above the ground. As is seen through the color scale, the simulated flow records a local maximum within the building complex (location 2), which coincides with the subjective appreciations of those who transit there frequently. There are strong recirculation zones inside the domain, linked to complex geometrical patterns, a well-documented feature in urban wind [1,56], driven by pressure gradients produced when the flow interacts with obstacles. Also, the simulation displays strong turbulence inside the building complex (large perturbations in wind speed, standard deviation $\sigma(U) \sim 1$ m/s, Video link1).

In order to have a partial validation of these results we carried out a small field campaign in the building complex, installing 4 sonic anemometers (R.M. Young Model 8100) and 2 conventional anemometers (locations shown in Fig. 4), aimed at identifying the existence of a local maximum in the flow velocity. Anemometer B was located on the roof of one of the buildings, and was used to verify the main wind conditions, while the others were located 3 m above the ground.

The data generated by anemometers 1, 2 and 3 during an afternoon that fulfills the southwest wind condition are shown in Fig. 5. The magnitude of the wind measured by anemometer 2 exceeded, at all times, the records of anemometers 1 and 3, consistent with the averaged results of the simulation. This characteristic is also present in other afternoons that fulfill the southwest wind condition (not shown).

The average velocity vectors recorded by the anemometers are shown in Fig. 4 as vectors displaced from the location of measurement. In the flow acceleration zones (locations 2 and 3), the simulated values correctly approximate the measured values in magnitude ($\sim$2 and $\sim$1.5 m/s respectively), and in direction. On the contrary, the simulated values at point 1 differ from measurements, that record low-intensity counter flow winds. These differences may be attributed to obstacles that were not included in the simulation, in particular a 3 m terrace located in front of the central building that appears to be responsible for the flow perturbations in this area. The larger variability at point 1 is evident when comparing the frequency distribution of the wind directions measured by the anemometers at different locations (Fig. 6). A clear prevailing wind direction is not seen at location 1, in contrast to what happens at locations B, 2 and 3. U_x (velocity component aligned with the main distribution of buildings) statistics from the simulation coincide with those from data sampled by sonic anemometers, confirming the existence of intense turbulence inside the building complex (Table 1).

Even if the evidence of this particular test case is qualitative at best it supports the validity of using DES type simulations to solve the atmospheric flow around complex geometries, and demonstrates the ability of the *snappyHexMesh* tool to generate fully operational complex meshes, that was our primary objective for this section of the work.

3.2. Buoyant cases

None of the cases above does consider thermal effects on the flow, as they focus on the interaction of the flow with obstacles and complex geometries. The next step, therefore, was to validate the results of buoyant cases. We selected two cases, first a simple

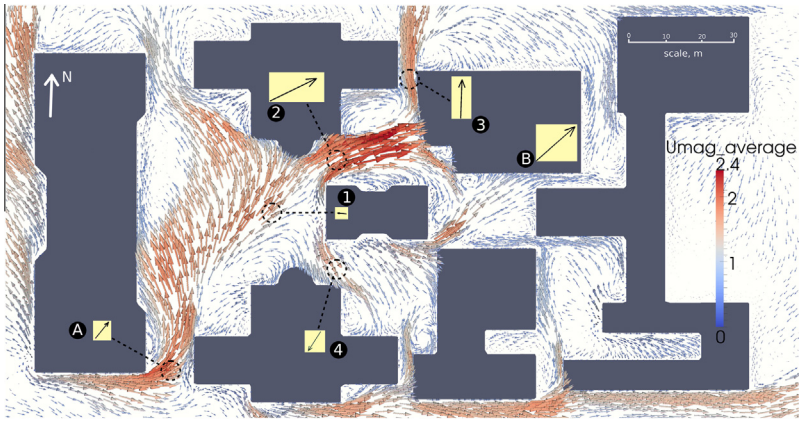

Fig. 4. Simulation results inside the FCFM buildings complex (mean velocity vectors 3 m above ground, m/s). Mean velocity vectors recorded by anemometers are shown as displaced vectors. Segmented circles indicate the location of sonic anemometers 1, 2, 3 and 4, and conventional anemometers A and B.

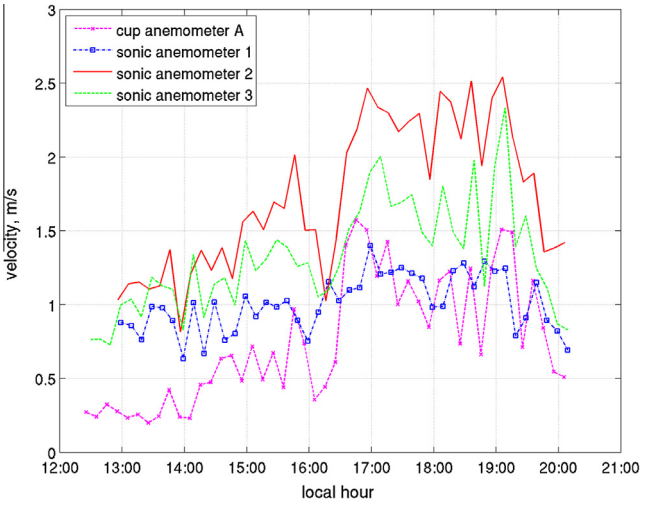

Fig. 5. Anemometer data recorded during one of the days sampled, 10 min mean horizontal velocity magnitude (m/s) versus local time.

experimental one with detailed data available, and then a complex atmospheric case well documented in the literature. We will specifically focus our attention in the second case, because its conditions are similar to those affecting large open pit mines under intense solar insolation, as Chuquicamata.

3.2.1. Simple experimental case

We used experimental data from the ERCOFTAC library, with case 79, Turbulent Natural Convection in an Enclosed Tall Cavity [57]. The case consists of a closed rectangular cavity 2.18 m high by 0.076 m wide by 0.52 m in depth, whose lateral walls are subjected to 20 °C differential heating (ΔT), with a Rayleigh

Table 1
Standard deviation (σ, m/s) of U_x (velocity component aligned with the main distribution of buildings) in selected points inside the domain (locations shown in Fig. 4). Field data (sonic anemometers sampled each 0.25 s) and simulation data (time step 0.05 s, resampled each 0.25 s).

Point	Standard deviation $\sigma(U_x)$, m/s	
	Measured	Simulated
1	0.7	0.6
2	0.6	0.5

Number, based on the width of the cavity (L), of $Ra = 0.86 \times 10^6$. The boundary conditions used in this case are particularly simple, since we deal with an enclosed flow: zero velocity at walls, fixed temperature at vertical walls, and adiabatic upper and lower horizontal walls. We used a mesh of $64 \times 52 \times 218$ grid points and a time step of 0.001 s for a full simulation time of 20 min (reaching a statistically stationary flow). Similar results were obtained refining the mesh in each axis. Wall normal dimensions between $y_1^+ = 5$ and $y_1^+ = 20$ adjacent to the surface were used. The buoyancy velocity (V_o) was calculated based on the width of the cavity (L):

$$V_o = \sqrt{g\beta L(\Delta T)} = 0.2\text{m/s} \tag{16}$$

with β the thermal expansion coefficient. V_o scales as the vertical mean velocity near the walls. We can define a reference time as the total height of the cavity divided by the calculated buoyancy velocity: $t_{ref} = H/V_o \sim 10$ s, and introduce a dimensionless time $\tau = t/t_{ref}$.

In Fig. 7 we compare our results (100 s averages ($\tau = 10$) at final time ($\tau = 120$)) with temperature and velocity experimental data for horizontal sections between both walls at different heights above the bottom. Different combinations of final and averaging times have been tested to ensure that the final convergent time-averaged

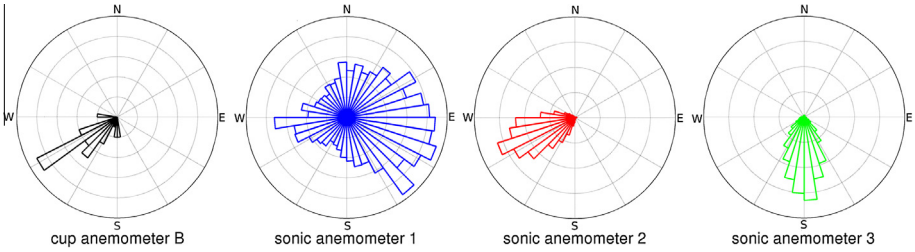

Fig. 6. Wind roses of recorded data, location B (over the roof) and sonic anemometers 1, 2 and 3 respectively (locations shown in Fig. 4).

results were attained. The model is capable of correctly simulating the distribution of the temperature (hotter wall to the right and colder to the left), as well as the circulation caused by the changes in density (rising along the right wall, falling along the left wall). The asymmetry in the distribution of velocity and temperature generated by the upper and bottom boundaries can be distinguished in the results (lower velocity of the flow that impacts against the boundary). In contrast, at the center of the cavity, far from the upper and lower boundaries, the profiles are rotationally symmetrical. Our DES results are similar to those obtained by Hsieh et al. [58] using unsteady RANS with a low-Re k–ε model (Figs. 3 and 4 of that work).

3.2.2. Turbulence in the atmospheric boundary layer

Finally, we studied the efficiency of the solver in simulating buoyant flows on a large-scale, following the work by Moeng and Sullivan [8] and Churchfield et al. [59] (hereafter referred to as MS94 and CH10, respectively). Both works used LES (pseudo-spectral solver in MS94, finite volume solver in CH10), to accurately simulate the atmospheric boundary layer under different combinations of wind shear and buoyancy forces.

The study case corresponds to a horizontal domain of 5×5 km and 2 km height. The results shown correspond to a mesh of $160 \times 160 \times 128$ grid points, like that used in CH10, although

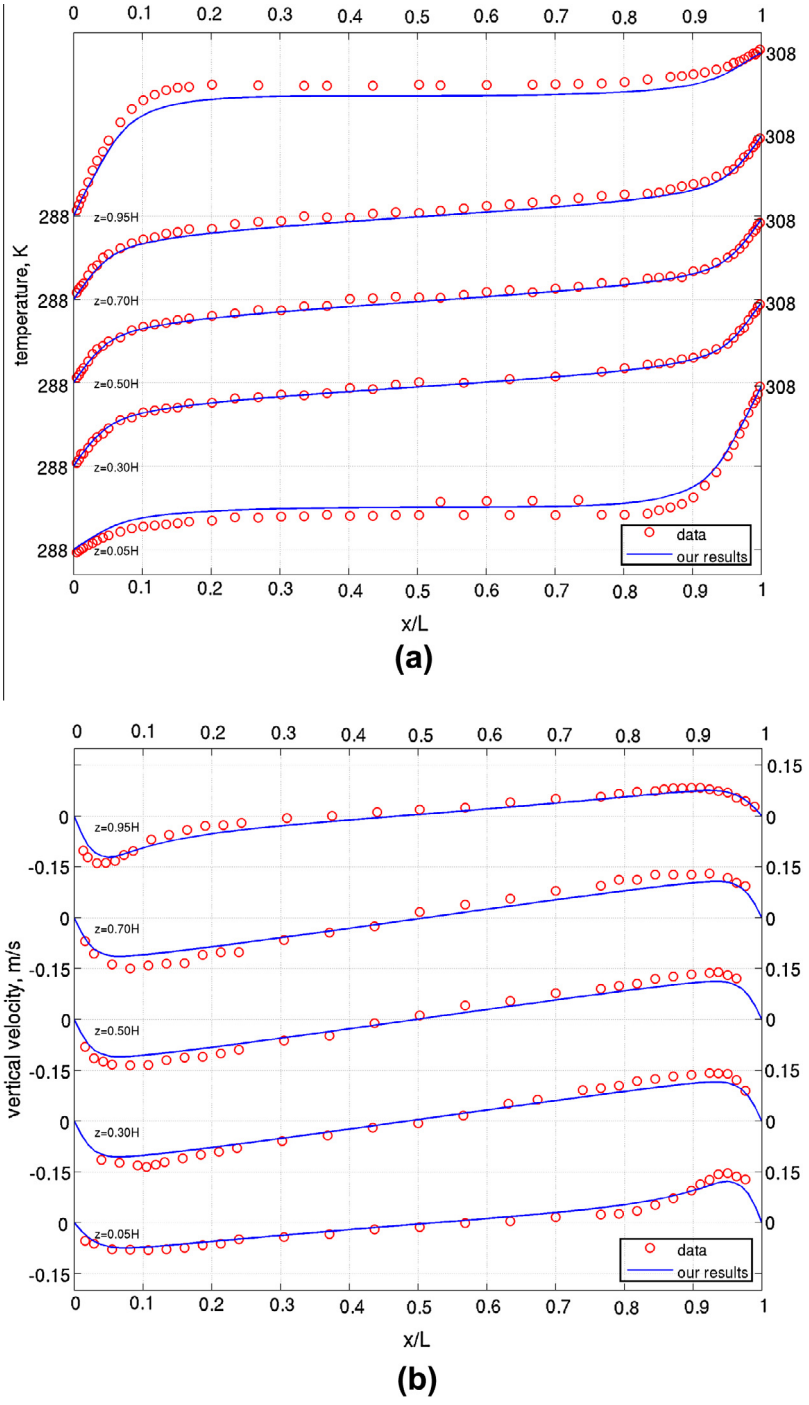

Fig. 7. (a) Temperature (K) and (b) vertical velocity (m/s), in a line linking cold and hot walls at different heights, simulation (blue line) v/s ERCOFTAC experimental data (red circles). H is the total height of the closed cavity and L is the separation between the walls at a different temperature. (For interpretation of the references to color in this figure legend, the reader is referred to the web version of this article.)

similar results were obtained with a $96 \times 96 \times 96$ mesh, like that used in MS94. A fixed surface heat flux of 240 W/m^2 and a 10 m/s wind speed above 300 m are prescribed. u_*, the friction velocity, has a value of 0.56 m/s, while the convective temperature scale ($T_* = q_s/w_*$) is 0.12 K. The initial potential temperature profile has a constant value of 300 K up to 937 m, followed by an 8 K increase in the next 167 m, and a constant 0.003 K/m gradient up to the top of the domain. We employ cyclic lateral boundary conditions in both horizontal directions. The upper boundary conditions are free-slip and maintain a constant potential temperature gradient, specified to be that of the initial capping inversion profile (0.003 K/m). To facilitate the initial development of turbulence the initial velocity field was perturbed as suggested by de Villiers [28], introducing periodic perturbations along the x and y-axes through sine and cosine functions. The time step used was 0.25 s, for a full simulation time of 4 h. In this case we included Coriolis in the simulation (Eq. (4)) and kept a 10 m/s geostrophic wind above the boundary layer.

The time evolution of velocity and potential temperature profiles are shown in Fig. 8 (horizontal averages over the entire computational domain). The convective turbulent mixing generated by buoyancy occurs below the first inversion, generating a clearly identifiable convective boundary layer (CBL). In the case of velocity profiles our results compare well with those reported in CH10, showing the development of a boundary layer with less wind than the layer above it, due to the turbulent momentum transfer to the surface. The profiles of potential temperature show the heating of the air below the first inversion, the increase of the boundary layer height (after 9000 s $z_i \sim 980$ m), and the entrainment at the top of this layer. Also evident is a weak stabilization of the temperature profile in the upper half of the CBL. These features are similar to those documented by Moeng [60], Stull [61] and Wyngaard [62]. We integrate the net heating of the temperature profile to estimate the average heat flux received by the entire volume:

$$\overline{Q} = \frac{1}{t_f} \int \rho c_p (\theta_f - \theta_0)\, dz, \tag{17}$$

where t_f is the final time, c_p the specific heat of dry air, ρ the air density profile, and θ_f and θ_0 the final and initial vertical profiles of potential temperature (horizontal averages over the entire computational domain). We obtain $\overline{Q} \sim 243$ W/m^2, very close to the imposed surface heat flux (240 W/m^2).

The existence of powerful thermals, which favor the mixing and occur over the entire domain, is clearly shown in an animation of a passive tracer released from the surface (Fig. 9 and Video link). The full model time series of vertical velocity and potential temperature in a point at 500 m above the ground in the center of the domain, are shown in Fig. 10a and b. The presence of thermals is evident in Fig. 10a, by maximum vertical velocities that reach up to 4 m/s. The root mean square value of these perturbations ($\sigma_w \sim 1.6$ m/s) is of the same scale as the convective velocity scale,

$$w_* = \left(\frac{g}{\theta_0} q_s z_i\right)^{1/3} \sim 2 \text{ m/s}, \tag{18}$$

in accordance to Deardorff [63]. The heating of the air below the inversion is reflected in the gradual increase of potential temperature shown in Fig. 10. In the evolution of vertical velocity and temperature an initial delay is observed, attributable to the time taken by the perturbation induced by the surface heat flux in reaching the level where the data was taken.

Fig. 11 shows the spectra of energy contained within the horizontal velocity fluctuations, u_h, the vertical velocity, w, and the potential temperature, θ, at height $z/z_i = 0.5$ [59,64]. To create the energy spectra we used a 2D fast Fourier transform to calculate the 2D energy spectrum and then we computed the spectral energy contained within shells of constant wavenumber magnitude $\left(k_h = \sqrt{k_1^2 + k_2^2}\right)$ [62]. In red we plot the slope of the Kolmogorov spectrum ($k_h^{-5/3}$), which is partially followed by our results in the inertial range. However, they do not follow the $-5/3$ slope as well as the spectra of Khanna and Brasseur [64], probably because we are using a finite volume formulation, more numerically diffusive than a pseudo-spectral solver (CH10).

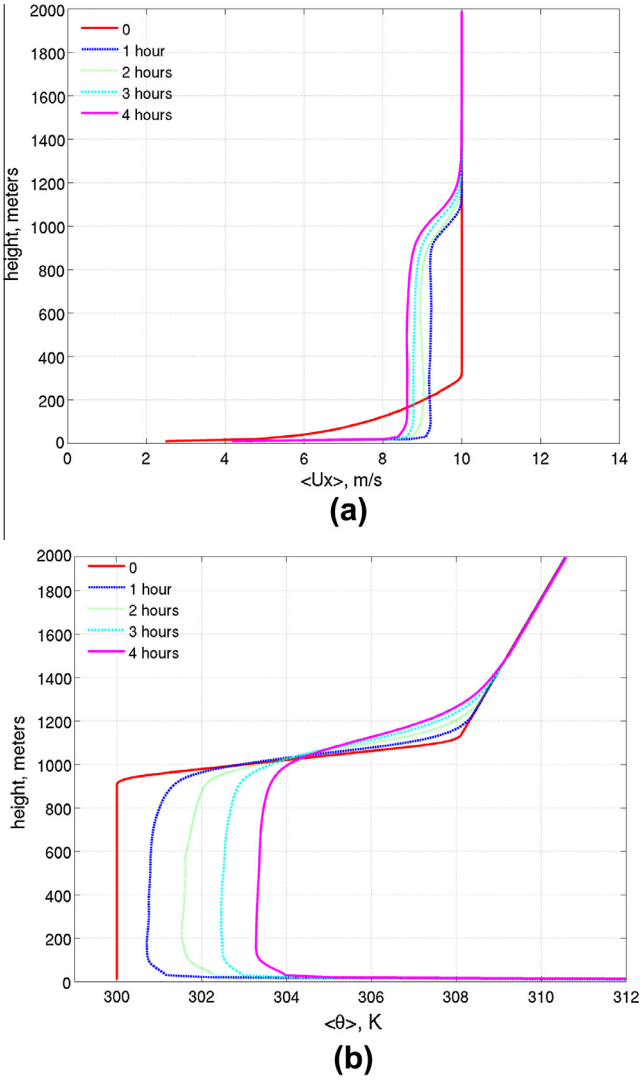

Fig. 8. Time evolution of vertical mean profiles (horizontal average over the entire computational domain). (a) Horizontal velocity, m/s. (b) potential temperature, K.

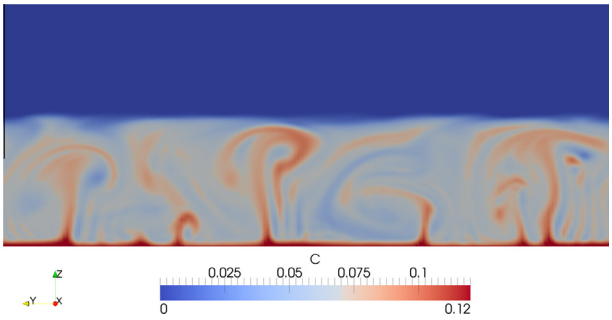

Fig. 9. Instantaneous concentration of a passive tracer released from the surface for a y–z plane in the middle of the domain.

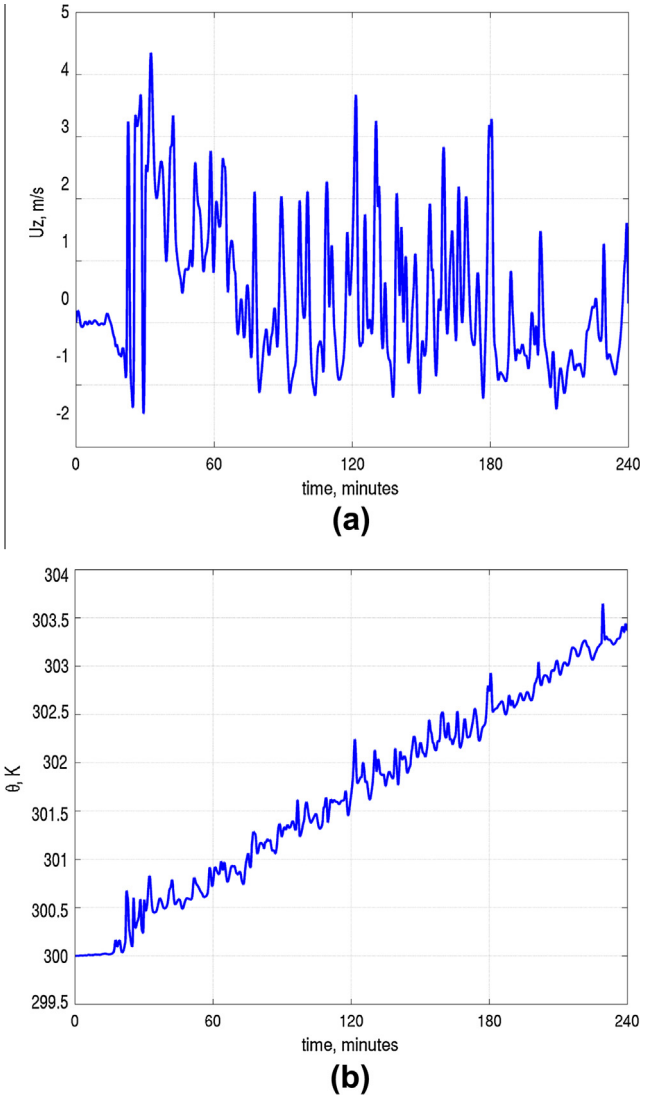

Fig. 10. Time evolution of selected variables at 500 m above ground at the center of the domain, data sampled at each time step (0.25 s). (a) Vertical velocity, m/s. (b) Potential temperature, K.

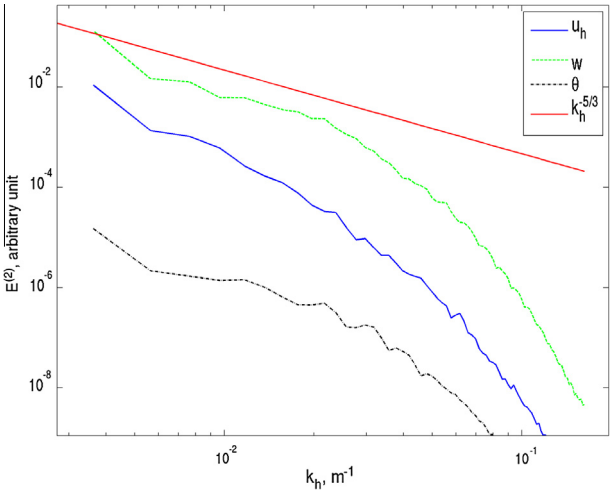

Fig. 11. Two-dimensional variance spectra of $u_h = \sqrt{u^2 + v^2}$, w, and θ over an horizontal plane at $z/z_i = 0.5$.

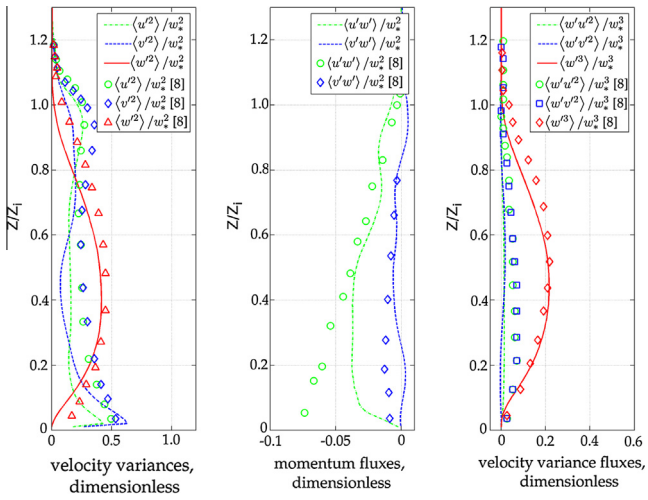

Fig. 12. Nondimensional vertical profiles of horizontally-averaged resolved velocity variance, momentum fluxes and velocity variance fluxes, compared to results of Moeng and Sullivan [8]. We have normalized the results by the convective velocity scale w_*.

Important turbulent statistics of our DES simulation results (velocity variances, momentum fluxes and velocity variance fluxes), comparable with those of MS94 and CH10, are shown in Fig. 12. Our statistics show good agreement with these previous studies, especially those of vertical velocity, controlled by the buoyancy produced by the heat flux. In particular, as described in CH10, vertical velocity variance, $\langle w'w' \rangle$, peaks around $z/z_i = 0.4$, vertical velocity variance flux, $\langle w'w'w' \rangle$, is greater than the other variance fluxes, and horizontal velocity variances, $\langle u'u' \rangle$ and $\langle v'v' \rangle$, peak near the base of the capping inversion and near the surface. The differences observed in horizontal velocity statistics close to the ground are attributable in part to our use of specific wall functions different than those used in the other works, which were needed in order to incorporate complex geometries in our simulations. Furthermore, MS94 data include the sub-grid-scale contribution, while our results consider only resolved variances. Also, our finite-volume solver is inherently more dissipative than the pseudo-spectral solver used in MS94. Spectral methods are not, however, easy to apply for complex domains, as the one we are interested in simulating, so at the beginning of this work we opted for a finite-volume approach, as that used by OpenFOAM. Perhaps the selection of higher order numerical schemes could

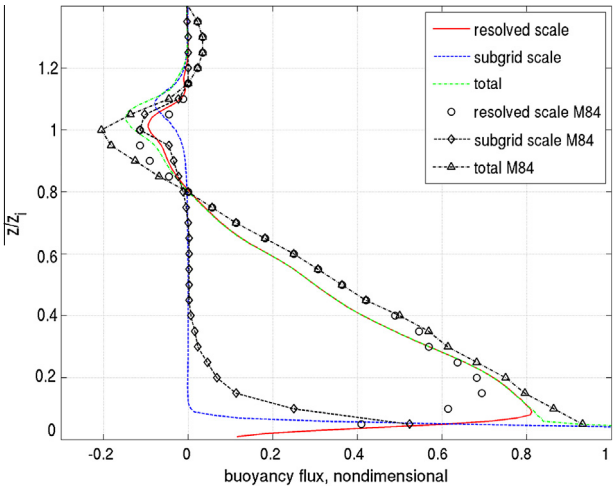

Fig. 13. Nondimensional resolved, subgrid and total buoyancy flux, compared to results from Moeng [60] (M84).

avoid this problem, but could introduce stability problems when used in complex geometries. There are also two more sources for the differences between our results and the references. (1) The DES solver with RANS in the near wall regions damps the turbulence fluctuations. A few published papers (e.g. [65]) report some ways to enhance such fluctuations at the interface of the RANS and LES regions. (2) In MS94 a modified wall model is used to take account of the rough wall effects (see Moeng [60]).

The important process of the entrainment at the top of the CBL can be identified by means of the buoyancy flux vertical profile (Fig. 13). The resolved buoyancy flux correctly approximates the reference simulations. In particular, the entrainment is shown by the negative value of the buoyancy flux at the CBL top, with differences from the references originating probably in the subgrid scale values. In particular, these differences may be linked to the fact that we used a fixed value of the turbulent Prandtl number, Pr_t, not modified as a function of the level of stratification. We expect to investigate this idea in future simulations. Since our grid has higher resolution than that used in the references the increase of the subgrid scale contribution occurs closer to the ground.

4. Conclusions

We have described the development of a numerical solver implemented in *OpenFOAM* for investigating complex atmospheric flows that include developed turbulence, stratification, thermal buoyancy and complex geometry. The model includes specific boundary and initial conditions needed to simulate the problem and uses a DES approach, combining LES to correctly simulate developed turbulence with RANS to solve the flow close to walls. Density was included as a variable in the system of equations to improve the treatment of stratification and buoyancy. To incorporate complex geometries we used the *snappyHexMesh* tool, obtaining fully operative meshes. We used different case studies to test our framework at different levels. Simple non-buoyant experimental cases were used to check the simulation of recirculation and the

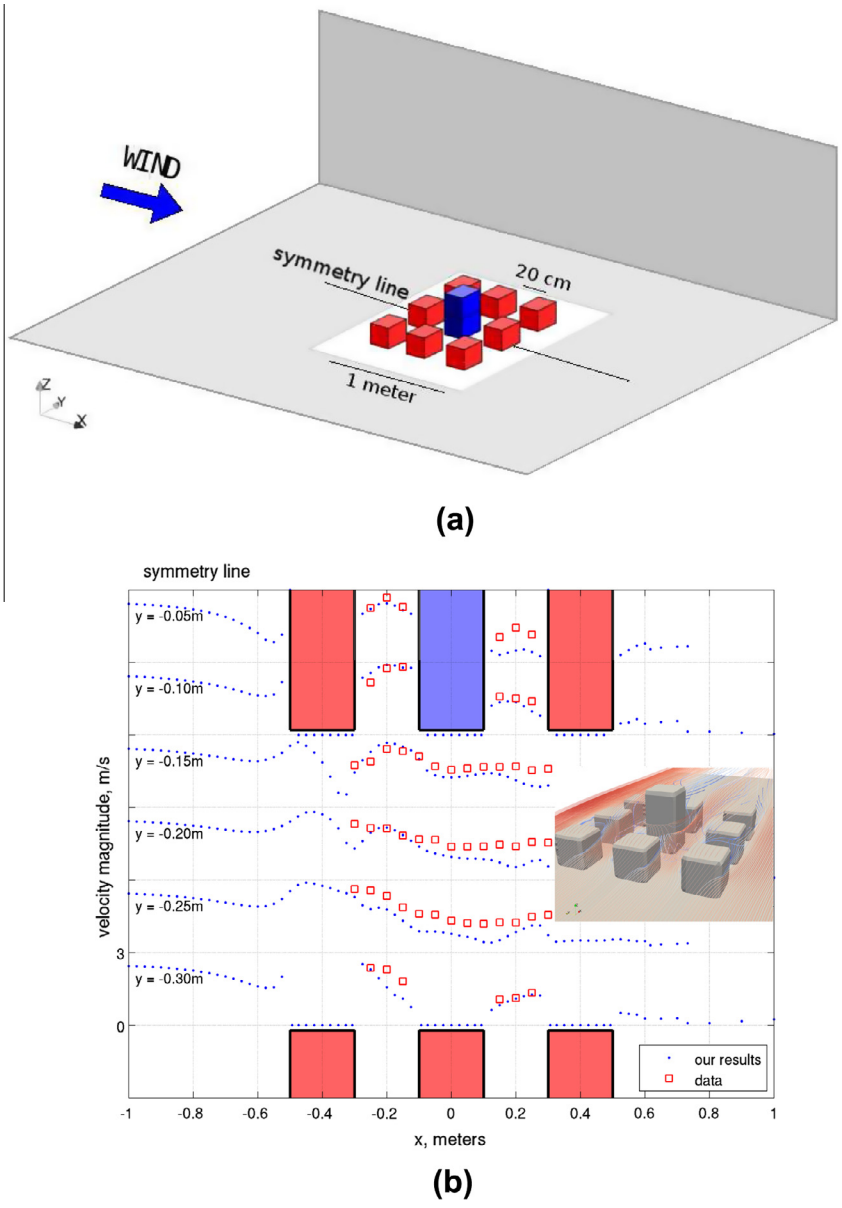

Fig. B.14. Simple city blocks (side 20 cm). (a) Experimental test case, AIJ, adapted from [4]. (b) Simulation (blue dots) v/s AIJ experimental data (red squares). Velocity magnitude (m/s) in lines at different positions with respect to *y*-axis, on a horizontal plane near the ground ($z = 0.02$ m) (bilateral symmetry across symmetry line). Geometrical scales were modified to improve data representation. Inlet wind speed aloft ~6 m/s. (For interpretation of the references to color in this figure legend, the reader is referred to the web version of this article.)

perturbation in the wake of obstacles. More complex large scale non-buoyant cases were used to study the ability of the *snappyHexMesh* tool to generate detailed complex meshes fully integrated to the numerical formulation used by *OpenFOAM*. Finally, buoyancy was introduced using first a simple experimental case, and then studying in detail a well documented atmospheric case. Both buoyancy and stratification demonstrated being well simulated, in agreement with previous observational and modelling results. While DES and URANS techniques showed similar results in simple non-buoyant cases, in strongly buoyant cases the ability of DES to solve developed turbulence was not replicated by URANS techniques. Although there are still many points to improve, such as the efficiency of the subgrid model or the treatment close to the walls, it was possible to show that the model and the particular boundary and initial conditions implemented in *OpenFOAM* for this work can deal with the complex multiphysical problem that implies modelling atmospheric flows close to a complex ground.

Despite its limitations and it still being a technique under development, DES is a good alternative for making use of the advantages offered by LES when modelling turbulent atmospheric flows, without having to pay the high computing cost that would be implied by using this technique in complex geometries or topographies. Much research is still required to define the most efficient ways of integrating the RANS models that are so well-known in wind engineering to the LES simulations, in particular when considering convective atmospheric cases, but tools such as those allowed by the *OpenFOAM* platform will be of great help in this development. The modular characteristic of *OpenFOAM* allows equations and submodels to be added to a principal model as the simulation becomes more complex. This makes it advisable to address the modelling of complex atmospheric flows through a methodology like that used in this work, incorporating physical processes to the simulation progressively.

Given the good results obtained when simulating the convective case, in the second part of this work we will apply this solver to the study of the internal circulation developing in large open pit mines. We will simulate the particular case of Chuquicamata, one of the largest open pit mines in the world, located in northern Chile. In this mine the dispersion and exit of contaminants are controlled by the convective conditions inside the cavity [17].

Acknowledgments

This work was carried out during the doctoral research of the first author, with the support of Conicyt under Grant "Beca para Estudios de Doctorado Nacional". *Powered@NLHPC*: This research was partially supported by the supercomputing infrastructure of the NLHPC (ECM-02), Center for Mathematical Modeling CMM, Universidad de Chile.

Appendix A. Abbreviations and symbols

ABL, Atmospheric Boundary Layer; CAE, Computer Aided Engineering; CBL, Convective Boundary Layer; CFD, Computational Fluid Dynamics; DES, Detached Eddy Simulation; DNS, Direct Numerical Simulation; FCFM, School of Physical and Mathematical Sciences of the University of Chile; LES, Large Eddy Simulation; NLHPC, National Laboratory for High Performance Computing; RANS, Reynolds Average Navier Stokes; RNG, Renormalization Group; SGS, Subgrid Scale; STL, stereolithography; URANS, Unsteady Reynolds Average Navier Stokes; WRF, Weather Research and Forecasting; ∇, gradient operator (m^{-1}); $\nabla\cdot$, divergence operator (m^{-1}); ∇p^*, external forcing (Pa/m); Δ, delta, filter width; λ, potential temperature lapse rate (K/m); $\vec{\Omega}$, earth rotation angular velocity (rad/s); α, α_{sgs}, α_t, thermal diffusivity, subgrid scale, effective SGS (kg/(ms)); $\frac{D}{Dt}$, total derivative; $\frac{\partial}{\partial t}$, partial derivative; δ_{ij}, Kronecker delta; κ, von Karman constant; σ, standard deviation; θ, θ_1, θ_0, θ_f, potential temperature, at level 1, initial, final (K); ρ, density (kg/m^3); ν, kinematic viscosity (m^2/s); μ, μ_{sgs}, dynamic viscosity, subgrid turbulent viscosity (Pa s); τ, dimensionless time; c_p, specific heat of dry air (J/(Kg K)); C, passive scalar; d, displacement height (m); e, specific internal energy (J/kg); $\vec{f_c}$, Coriolis force (N/m^3); f, variable; f_v, source; G, function; g, gravity acceleration (m/s^2); h, specific enthalpy (J/kg); k, turbulent kinetic energy (m^2/s^2); k, wavenumber (m^{-1}); n, exponent of the power law; p, p_o, p_1, pressure, reference pressure, at level 1 (Pa); Pr_t, Prandtl turbulent number; $\overline{Q}$, mean heat flux (W/m^2); q_s, kinematic heat flux at surface (K m/s); R, gas constant for dry air (J/(KgK)); Ra, Rayleigh number; $\mathbf{T}$, $\mathbf{T}_{sgs}$, stress tensor, subgrid scale stress tensor (kg/(ms^2)); T, temperature (K); T_*, convective temperature scale (K); t, t_f, time, final time (s); $U(z)$, U_s, horizontal velocity at height z, at height z_s (m/s); $\vec{U}$, $u_{i,j,k}$, velocity vector, components (m/s); U_x, component aligned with buildings (m/s); U_*, friction velocity (m/s); u_h, horizontal velocity $\sqrt{u^2+v^2}$ (m/s); u, v, w, velocity components, xyz (m/s); v, specific volume (m^3/kg); V_o, buoyancy velocity (m/s); w_*, convective velocity scale (m/s); y_1^+, distance in wall units between the centroid of the first cell and the wall assuming the y coordinate is normal to the wall; z, z_s, z_1, height, reference height, at level 1 (m); z_i, convective boundary layer height (m); z_o, roughness height (m).

Appendix B. Experimental non-buoyant test case

The third experimental test case considered corresponds to a complex geometry consisting of a set of nine obstacles (Takayoshi [54] and Yoshie et al. [55], Fig. B.14). Given the complexity of the geometry of this case, with different-sized obstacles distributed over a large domain, we used the *snappyHexMesh* tool to generate the mesh, refining the most complex zones by the use of *snappyHexMesh* controls, to produce cells with wall normal dimensions of between $y_1^+ = 10$ and $y_1^+ = 100$ adjacent to the surface. Different meshes were used until obtaining grid independent results. The inlet profile of velocity was adjusted using the experimental data provided by the library (~6 m/s wind speed aloft), using the mapping technique available in OpenFOAM to initiate turbulence. Part of the results obtained are seen in Fig. B.14, corresponding to a horizontal plane close to the ground (10 s averages after 2 min of simulation, although different combinations of final and averaging times have been tested to ensure that the final converged time-averaged results were attained). The simulation results are consistent with experimental data. In particular, the simulation was able to solve the flow established between the obstacles, and in the wake generated by them. Also, our DES results are in accordance with the distribution of turbulence energy around a simple city block reported by Takayoshi [54] using RANS simulations.

Appendix C. Supplementary material

Supplementary data associated with this article can be found, in the online version, at http://dx.doi.org/10.1016/j.compfluid.2013.04.029.

References

[1] Fernando HJS, Zajic D, Sabatino SD, Dimitrova R, Hedquist B, Dallman A. Flow, turbulence, and pollutant dispersion in urban atmospheres. Phys Fluids 2010;22. 051301.
[2] Franke J, Hellsten A, Schlünzen H, Carissimo B. Best practice guideline for the CFD simulation of flows in the urban environment. COST action 732 quality assurance and improvement of microscale meteorological models; 2007.
[3] Kondo H, Horiuchi K, Hirano Y, Maeyama N, Ogata K, Iizuka S, et al. Attempt to make guideline to use CFD model for atmospheric environmental assessment

in urban area in Japan. In: The seventh international conference on urban climate, 29 June–3 July 2009, Yokohama, Japan; 2009.
[4] Tominaga Y, Mochida A, Yoshie R, Kataoka H, Nozu T, Yoshikawa M, et al. AIJ guidelines for practical applications of CFD to pedestrian wind environment around buildings. J Wind Eng Ind Aerodynam 2008;96:1749–61.
[5] Moin P, Mahesh K. Direct numerical simulation: a tool in turbulence research. Annu Rev Fluid Mech 1998;30:539–78.
[6] Franke J, Hirsch C, Jensen A, Krüs H, Schatzmann M, Westbury P, et al. Recommendations on the use of CFD in wind engineering. WG2 dissemination; 2004.
[7] Fritts DC, Goldstein D, Lund T. High-resolution numerical studies of stable boundary layer flows in a closed basin: evolution of steady and oscillatory flows in an axisymmetric Arizona meteor crater. J Geophys Res 2010;115. D18109.
[8] Moeng CH, Sullivan P. A comparison of shear- and buoyancy-driven planetary boundary layer flows. J Atmos Sci 1994;51(7):999–1022.
[9] Brasseur JG, Wei T. Designing large-eddy simulation of the turbulent boundary layer to capture law-of-the-wall scaling. Phys Fluids 2010;22. 021303.
[10] Bechmann A, Sorensen N, Johansen J, Vinther S, Nielsen B, Botha P. Hybrid RANS/LES method for high Reynolds numbers. Applied to Atmospheric Flow over Complex Terrain. J Phys: Conf Ser 2007;75:012054.
[11] Lee SH, Kim SW, Angevine WM, Bianco L, McKeen SA, Senff CJ, et al. Evaluation of urban surface parameterizations in the WRF model using measurements during the Texas Air Quality Study 2006 field campaign. Atmos Chem Phys 2011;11:2127–43.
[12] Han J, Pan HL. Revision of convection and vertical diffusion schemes in the NCEP global forecast system. Weather Forecast 2011;26:520–33.
[13] Wyngaard JC. Toward numerical modeling in the "Terra Incognita". J Atmos Sci 2004;61:1816–26.
[14] Chen F, Kusaka H, Bornstein R, Ching J, Grimmond C, Grossman-Clarke S, et al. The integrated WRF/urban modeling system: development, evaluation, and applications to urban environmental problems. Int J Climatol 2011;31:273–88.
[15] Spalart PR, Jou W, Strelets M, Allmaras SR. Comments on the feasibility of LES for wings, and on a hybrid RANS/LES approach. In: Proceedings of 1st AFOSR international conference on DNS/LES; 1997. p. 137–47.
[16] Weller H, Tabor G, Jasak H, Fureby C. A tensorial approach to computational continuum mechanics using object-oriented techniques. Comput Phys 1998;12(6):620–31.
[17] Barkan J, Alpert P. The linkage between solar insolation and dust in the major world deserts. Open Atmos Sci J 2010;4:101–13.
[18] OpenCFD. User and programmer's guide. OpenFOAM; 2009. Version 1.6.
[19] García M, Boulanger P. Low altitude wind simulation over Mount Saint Helens using NASA SRTM digital terrain model. In: Proceedings of the third international symposium on 3D data processing, visualization, and transmission (3DPVT'06); 2006.
[20] Hussein AS, El-Shishiny H. Influences of wind flow over heritage sites: a case study of the wind environment over the Giza Plateau in Egypt. Environ Modell Software 2009;24:389–410.
[21] García M, Boulanger P, Duque J, Giraldo S. CFD analysis of the effect on buoyancy due to terrain temperature based on an integrated DEM and Landsat infrared imagery. Ing Cienc 2008;4(8):65–84.
[22] Pedruelo X. Modelling of wind flow over complex terrain using openfoam. Master's thesis. Department of Technology and Built Environment, University of Gavle; 2009.
[23] Churchfield MJ. A description of the OpenFOAM solver buoyantboussinesqpisofoam. National Renewable Energy Laboratory, National Wind Technology Center; 2010.
[24] Issa R. Solution of the implicitly discretised fluid flow equations by operator-splitting. J Comput Phys 1985;62:40–65.
[25] Issa R. The computation of compressible and incompressible recirculating flows by a non-iterative implicit scheme. J Comput Phys 1986;62:66–82.
[26] Oliveira P, Issa R. An improved PISO algorithm for the computation of buoyancy-driven flows. Numer Heat Transfer 2001;Part B, 40:473–793.
[27] Demirdzic I, Lilek Z, Peric M. A collocated finite volume method for predicting flows at all speeds. Int J Numer Methods Fluids 1993;16:1029–50.
[28] de Villiers E. The potential of large eddy simulation for the modeling of wall bounded flows. PhD thesis. Thermofluids Section, Department of Mechanical Engineering, Imperial College of Science, Technology and Medicine; 2006.
[29] Yoshizawa A, Horiuti K. A statistically-derived subgrid-scale kinetic energy model for the large-eddy simulation of turbulent flows. Phys Soc Jpn J 1985;54:2834–9.
[30] Satoh M. Conservative scheme for the compressible nonhydrostatic models with the horizontally explicit and vertically implicit time integration scheme. Mon Weather Rev 2002;130:1227–45.
[31] Akmaev R, Juang HMH. Using enthalpy as a prognostic variable in atmospheric modelling with variable composition. Quart J R Meteorol Soc 2008;134:2193–7.
[32] Pino M, Piomelli U, Candler G. Subgrid-scale models for compressible large-eddy simulations. Theor Comput Fluid Dyn 2000;13:361–76.
[33] Porté-Agel F, Pahlow M, Meneveau C, Parlange MB. Atmospheric stability effect on subgrid-scale physics for large-eddy simulation. Adv Water Resour 2001;24:1085–102.
[34] Huang HY, Stevens B, Margulis SA. Application of dynamic subgrid-scale models for large-eddy simulation of the daytime convective boundary layer over heterogeneous surfaces. Bound-Layer Meteorol 2007;126:327–48.
[35] Wang BC, Yee E, Yin J, Bergstrom DJ. A general dynamic linear tensor-diffusivity subgrid-scale heat flux model for large-eddy simulation of turbulent thermal flows. Numer Heat Transfer, Part B 2007;51:205–27.
[36] Vdovin A. Radiation heat transfer in Openfoam. Final Assignment for the Course CFD with OpenSource Software; 2009.
[37] Modest MF. Radiative heat transfer. 525 B Street. Suite 1900, San Diego, California 92101-4495, USA. Academic Press; 2003.
[38] Savijarvi H. Radiative and turbulent heating rates in the clear-air boundary layer. Quart J R Meteorol Soc 2006;132:147–61.
[39] Lim H, Yu T, Glimm J, Li X, Sharp DH. Subgrid models for mass and thermal diffusion in turbulent mixing. Report, Los Alamos National Laboratory; 2009.
[40] OpenCFD. OpenFoam Advanced Training, Version 1.7.x; 2010.
[41] Shi Y, Feng X, Wei F. Three-dimensional nonhydrostatic numerical simulation for the PBL of an open-pit mine. Bound-Layer Meteorol 2000;94:197–224.
[42] Blocken B, Stathopoulos T, Carmeliet J. CFD simulation of the atmospheric boundary layer: wall function problems. Atmos Environ 2007;41:238–52.
[43] Tabor G, Baba-Ahmadi M. Inlet conditions for large eddy simulation: a review. Comput Fluids 2010;39:553–67.
[44] Xie ZT, Castro IP. Efficient generation of inflow conditions for large eddy simulation of street-scale flows. Flow Turbul Combust 2008;81:449–70.
[45] Baba-Ahmadi M, Tabor G. Inlet conditions for LES using mapping and feedback control. Comput Fluids 2009;38:1299–311.
[46] Silvester S, Lowndes I, Hargreaves D. A computational study of particulate emissions from an open pit quarry under neutral atmospheric conditions. Atmos Environ 2009;43:6415–24.
[47] Spalart PR. Detached-eddy simulation. Annu Rev Fluid Mech 2009;41:181–202.
[48] Maureira JC, Baeza C, Pérez T. Levque cluster user manual. Universidad de Chile; 2011. Major scientific and technological equipment for user facility centers.
[49] Jasak H. Parallelisation and scalability in OpenFOAM. International workshop on scalable engineering software, national science foundation, 2 June 2010; 2010.
[50] Lysenko DA, Ertesvag IS, Rian KE. Modeling of turbulent separated flows using OpenFOAM. Comput Fluids 2013;80:408–22.
[51] Lim H, Castro I, Hoxey R. Bluff bodies in deep turbulent boundary layers: Reynolds number issues. J Fluid Mech 2007;571:97–118.
[52] Lim HC, Thomas T, Castro IP. Flow around a cube in a turbulent boundary layer: LES and experiment. J Wind Eng Ind Aerodynam 2009;97:96–109.
[53] Mochida A, Tominaga Y, Murakami S, Yoshie R, Ishihara T, Ooka R. Comparison of various k–ε models and DSM applied to flow around a high-rise building. Report on AIJ cooperative project for CFD prediction of wind environment. Wind Struct 2002;5:227–44.
[54] Takayoshi T. The cross comparison of CFD results for flowfield around building models (part3), comparison of prediction accuracy for flowfield around building blocks. Architectural Institute of Japan, NII-Electronic Library Service; 2003.
[55] Yoshie R, Mochida A, Tominaga Y, Kataoka H, Yoshikawa M. Cross comparisons of CFD prediction for wind environment at pedestrian level around buildings. In: The sixth asia-pacific conference on wind engineering(APCWE-VI), Seoul, Korea; 2005.
[56] Zhang A, Gao C, Zhang L. Numerical simulation of the wind field around different building arrangements. J Wind Eng Ind Aerodynam 2005;93:891–904.
[57] Betts P, Bokhari I. Experiments on turbulent natural convection in an enclosed tall cavity. Int J Heat Fluid Flow 2000;21:675–83.
[58] Hsieh K, Lien F. Numerical modeling of buoyancy-driven turbulent flows in enclosures. Int J Heat Fluid Flow 2004;25:659–70.
[59] Churchfield MJ, Moriarty P, Vijayakumar G, Brasseur J. Wind energy-related atmospheric boundary layer large-eddy simulation using OpenFOAM. In: 19th Symposium on boundary layers and turbulence, Keystone, Colorado; August 2–6, 2010.
[60] Moeng CH. A large-eddy-simulation model for the study of planetary boundary-layer turbulence. J Atmos Sci 1984;41:2052–62.
[61] Stull RB. An introduction to boundary layer meteorology. Dordrecht, The Netherlands: Kluwer Academic Publishers; 1988.
[62] Wyngaard JC. Turbulence in the atmosphere. The Edinburgh Building, Cambridge CB2 8RU, UK: Cambridge University Press; 2010.
[63] Deardorff JW. Convective velocity and temperature scales for the unstable planetary boundary layer and for rayleigh convection. J Atmos Sci 1970;27:1211–3.
[64] Khanna S, Brasseur J. Three-dimensional buoyancy- and shear-induced local structure of the atmospheric boundary layer. J Atmos Sci 1998;55:710–43.
[65] Piomelli U, Balaras E, Pasinato H, Squires K, Spalart P. The inner-outer layer interface in large-eddy simulations with wall-layer models. Int J Heat Fluid Flow 2003;24:538–50.